IFIN-HH UPB ELI-NP

UNIVERSITY POLITEHNICA of BUCHAREST

Doctoral School in Engineering and Applications of Lasers and Accelerators

Doctoral Thesis
Summary

Non-destructive techniques for material inspection with quasi-monoenergetic gamma beams

Supervisor

CS1 Dr. Calin A. Ur

Autor

Gabriel V. Turturica

Bucharest 2020

Acknowledgements

I want to express my gratitude for those who helped me accomplish the results included in this thesis.

Firstly, I thank my supervisor Dr. Calin A. Ur, for providing me the opportunity to be part of this Ph.D. program. Under his guidance, we were able to define a clear path that laid the foundation for this thesis. I thank Dr. Violeta Iancu, my coordinator, who has been instrumental in my development as a Ph.D. student. She has always given me great advice that I sometimes overlooked and usually disagreed with, as it is in the student's nature. The results of our numerous discussions are present throughout all of the topics included in this work.

I want to thank my RA2 and RA4 colleagues for their help and assistance in the various problems encountered along the way. In particular, I would like to thank Dr. Catalin Matei for coordinating the HIGS data analysis and Alfio Pappalardo for all of his support related to the experimental parts of the thesis. I also want to thank Dr. Gabriel Suliman for his annoying self that motivated me to get better.

I want to thank the advisory committee members, Dr. Calin A. Ur, Prof. G. Cata-Danil, Dr. D. Balabanski, and Dr. N. Marginean, for their advice during the exams and scientific activity reports.

The work reported in the thesis was supported by the project Extreme Light Infrastructure Nuclear Physics (ELI-NP) Phases I and II, a project co-financed by the Romanian Government and European Union through the European Regional Development Fund.

Contents

Introduction

Non-destructive techniques based on photon attenuation have become standard procedures for cargo security screening. Improved security standards have raised the requirements in terms of material discrimination capabilities at the level of isotope specificity. One emerging technique capable of achieving these requirements is the nuclear resonance fluorescence (NRF) based isotopic mapping powered by quasi-monochromatic gamma-ray beams. The potential improvements in quasi-monochromatic gamma-ray beam quality achieved through the technological advancements of laser Compton scattering (LCS) machines may provide a solution for these requirements. Such a machine is under implementation at the Extreme Light Infrastructure – Nuclear Physics (ELI-NP) facility in Romania. The Variable Energy Gamma-ray (VEGA) system [1] aims to deliver quasi-monochromatic gamma-ray beams with exceptional parameters: small relative bandwidth ($\leq 0.5\%$), high spectral density (≥ 500 photons/s/eV), and high degree of linear polarization ($\geq 95\%$). The VEGA system targets fundamental physics, such as NRF and photoneutron reaction experiments, as well as practical applications [2–4]. The work presented in this thesis aims to investigate the potential advantages and drawbacks of employing LCS beams for non-destructive material inspections like NRF-based isotopic analysis.

The first two chapters outline the core elements required for understanding the NRF isotopic analysis, starting with the interaction of photons with matter, followed by a brief description of non-destructive techniques for material inspection. The following three chapters deliver insight regarding various conceptual and technical aspects of NRF based isotopic mapping.

The third chapter focuses on the implementation of two components with considerable influence on the spectral background for a typical NRF measurement, unavailable in the standard Geant4 framework. The first part covers the Geant4 implementation of the photon elastic scattering. This implementation was constructed by using a complete theoretical framework in order to account for the interference effects between the processes involved in the scattering cross-section. The second part of the chapter aims to close the gap between experimental and simulated data by including the additional constraint of temporal analysis to the simulation model. The purpose of this implementation was to assess the effect of pulse pile-up on the measured spectrum and to generate proper estimates for the counting rates, essential for giving realistic predictions.

The fourth chapter focuses on ROI selection techniques aimed to tackle the practical limitations associated with the relatively long measurement times of NRF isotopic analysis. The selected material discrimination method proposes a neural-network-based approach for dual-energy attenuation data analysis. The first part of the chapter covers a single-pixel dual-energy attenuation analysis. The purpose of this part is to demonstrate the advantage of the neural network approach to a classical method based on dual-energy reflex ratios. The second part of the chapter further extends the analysis to simulated 2D images. This section presents the comparison between a direct image analysis by using a convolutional neural network to a pixel-by-pixel approach for the dual-energy reflex.

The final chapter covers the particularities of the spectral and practical aspects of an NRF based isotopic analysis. The analysis assumes a high-performance HPGe array, as the detector, and a quasi-mono-energetic LCS beam, as the probing gamma-ray beam. A performance assessment of the detection array for a ^{238}U target employing the scattering configuration is made in the first part of the analysis. The second part of the chapter covers the results of a 2D isotopic analysis aimed at detecting and evaluating the ^{238}U content embedded in a selected high Z_{eff} region of the measured scene. Two elements were targeted for this analysis: the image quality, quantified by using the contrast-to-noise ratio as the metric, and the areal density evaluation capabilities. The final part covers the methods and tools required for beam energy and intensity measurements, essential requirements for an absolute evaluation of the isotopic areal density.

Chapter 1

Photon interaction with matter

In order to properly understand and design experimental setups targeted for non-destructive material inspection considerable knowledge of the processes involved in the photon-matter interaction is required. This chapter aims at describing the physical mechanisms that govern the interactions with the most substantial contribution to the attenuation of photons in matter.

1.1 Photon attenuation coefficient

The fundamental law of attenuation for the electromagnetic radiation in matter has the following form:

$$I = I_0 e^{-\mu x}\,, \tag{1.1}$$

where I_0 and I are the incident and transmitted intensity, μ is the mass attenuation coefficient, and x is the areal density defined as $x = \rho L$, with ρ as the material density and L the thickness of the absorber. The attenuation coefficient can be described as a function of the incident photon energy (E), the atomic number of the absorber (Z), and the density of the material (ρ). Attenuation coefficients, for each element and photon energies up to 100 GeV, can be obtained from XCOM: Photon Cross Sections Database [5].

The mass attenuation coefficient can also be expressed in terms of the interaction cross-section

$$\mu = \frac{N_0 \sigma}{A}\,, \tag{1.2}$$

where N_0 is Avogadro's number, σ is the interaction cross-section, and A is the atomic mass of the absorber. The interaction cross-sections can be expressed as the sum of the individual contributions of the different attenuation processes:

$$\sigma = \sigma_{pe} + \sigma_{pair} + \sigma_{Comp} + \sigma_{coh} + \sigma_{incoh} + \sigma_{NRF} + \dots \quad (1.3)$$

Based on the photons interaction mechanism, the individual components of the cross-section can be divided into two classes: non-resonant and resonant interactions.

1.2 Non-resonant attenuation

The components of the non-resonant attenuation can be split into two types of processes: photon absorption and photon scattering. Photon absorption is defined as the process in which the initial photon no longer exists after the interaction takes place and secondary particles are emitted in the process, e.g. the photoelectric effect or pair production. Photon scattering can be understood as an interaction from which the incident photon suffers a change in its direction of propagation or kinetic energy, e.g. Compton scattering and elastic scattering.

1.3 Resonant attenuation

The gamma decay of a nucleus is known to be an isotope specific process, in which photons are emitted following nuclear stabilization steps. The inverse process of photon emission is the photon absorption, which takes the nucleus to an excited state. The process of nuclear absorption followed by the emission of a photon is known as nuclear resonance fluorescence.

Chapter 2

Non-destructive techniques for material inspection

Over the last century, radiation-based methods have become standard procedures for material studies and characterization. The technical advancements in radiation production and detection have enabled the use of radiation for a board range of applications. This chapter will focus on photon-based radiography and will target non-resonant as well as resonant methods. The first section is dedicated to non-resonant radiography will cover the advantages and drawbacks of photon attenuation radiography and the additional improvements that can be achieved using dual-energy attenuation. The second part of the chapter will describe the NRF-based radiography, focusing on the experimental configurations and the proposed use cases of this method.

2.1 Non-resonant attenuation based methods

2.1.1 Photon attenuation radiography for cargo inspection

As it stands, photon attenuation radiography is an excellent tool to study the internal structure of an object. The method shows robust performances for an extensive range of atomic numbers and areal density values. Concerning the atomic number, the method does show shortcomings for complex materials, in which high Z components shield low Z components. On the areal density side, there are obvious limitations for objects that will completely attenuate the incident beam.

2.1.2 Effective atomic number evaluation using dual-gamma attenuation

One possible solution to the atomic number – areal density uncertainty is the dual-attenuation method. The method requires measuring the attenuation at two distinct photon energies. This measurement can give additional information regarding the atomic number and areal density of the object.

Dual-energy reflex

The most common method used for Z_{eff} evaluation is based on the relative dual-energy reflex [6]. The method requires a two-fold measurement process; reference runs in which no object is placed in between the gamma-ray source and the detector are followed by sample runs in which the attenuation of the gamma-rays is measured through an object. For the first step of the analysis, the ratio between the reference and sample signal is calculated as

$$R_c(E_i) = ln\left(\frac{V_0(E_i)}{V(E_i)}\right), \tag{2.1}$$

where V_0 is the reference signal (without object), and V is the sample signal (with object). The results obtained using formula (2.1) are then used to calculate the relative dual-energy reflex as

$$R = \frac{R_c(E_1)}{R_c(E_2)}, \tag{2.2}$$

where E_1 and E_2 are two distinct photon energies. The dependence of the effective atomic number to the dual-energy reflex can be described by using an equation as

$$Z_R = \left(\frac{a \cdot R + b}{c \cdot R + d}\right)^e, \tag{2.3}$$

where a, b, c, d, e are free parameters obtained using measurements of well-characterized samples.

Neural network approach

One of the simplest models is the plain-feed-forward neural network. Three types of elements define the structure of a plain-feed-forward network: input/output slots, connections, and neurons. The input/output slots are required in order to pass the information to/from the network. The connections are the elements that join all the structures of the system, e.g. input slot to neuron or neuron to neuron. Each connection has an associated variable, known as weight, that defines the importance of the connection between two structures. As a first operation, the neuron sums the products of the previous layer output with the corresponding weights and adds an additional bias to the sum. Afterward, the neuron passes the value obtained in the first step through an activation function. The value obtained after the activation function is passed on to the next layer. The weights and biases optimization is made during the back-propagation phase. The minimization procedure is done based on the error between the expected and the network predicted output based on a gradient decent algorithm.

2.2 Isotopic analysis using nuclear resonance fluorescence

Nuclear resonance fluorescence has been proposed as a non-destructive analysis technique that can provide an isotope-specific characterization of a sample object [7]. The method is based on the detection of resonant photons produced in the interaction of an incident beam with a sample material. The photons are generated in specific nuclear transitions that can be assigned to particular isotopes.

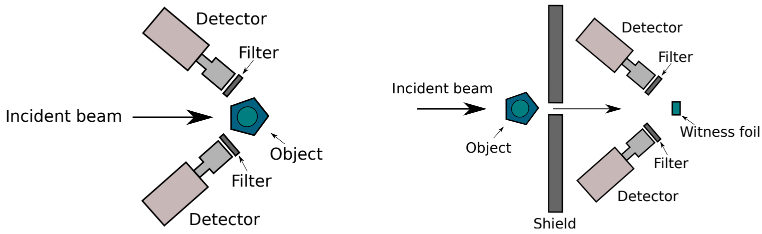

(a) Scattering configuration

(b) Transmission configuration

Figure 2.1: Experimental setups for NRF based isotopic analysis.

2.2.1 Scattering measurements

A schematic representation of the scattering configuration is shown in Figure 2.1a. In this configuration, detectors positioned around the object will record the beam-sample interaction. The photon flux reaching the detectors will be composed of resonant scattering, non-resonant scattering, and radioactive decays from the target. Background mitigation can be achieved by positioning the detectors at backward angles in order to reduce the non-resonant scattering contribution.

2.2.2 Transmission measurements

The transmission configuration, shown in Figure 2.1b, was proposed to solve some of the limitations of the scattering method [7]. In this configuration the beam is transmitted through the sample material and impinges on a witness target made out of the isotope of interest. The detection system is positioned around the witness target, which is shielded from the background generated by the sample material. One of the advantages of the transmission configuration is the improvement of the signal to background ratio due to the separation of the object from the detection system. Decoupling that is also practical if scanning of various sized objects is required as no adjustments are needed for the detection system.

Chapter 3

Geant4 developments to support active interrogation experiments

The design of an experimental setup plays an essential role in the expected outcome of a measurement. Currently, two methods are used in order to assess the outcome of an experimental measurement to aid the design process: analytical calculations and Monte Carlo simulations. As expected, neither one of these methods is ideal since both have specific advantages and drawbacks. The complexity of NRF measurements indicates that the best results for the outcome estimation problem can be obtained by using Monte Carlo simulations. This chapter presents the Geant4 implementations made in order to evaluate the results of NRF measurements by using a HPGe detector array coupled with a laser Compton scattering gamma-beam source.

3.1 Elastic scattering implementation

Elastic scattering implementations from typical particle transport codes, such as GEANT4 [8] or MCNP [9], are limited to Rayleigh scattering and ignore the rest of the processes [10]. This approximation is suited for low photon energies but yields considerable differences between simulation and experiment for energies above 1 MeV. Here, we extend the implementation of photon elastic scattering for energies up to 20 MeV to cover the energy domain of the future LCS source at the ELI-NP facility. In order to fully describe the elastic scattering of photons, the following processes have been considered: Rayleigh, nuclear Thomson, Delbrück, and nuclear resonance scattering.

3.1.1 Geant4 implementation of photon elastic scattering

Nuclear Thomson amplitudes were calculated based on the analytical formulas. The Rayleigh scattering amplitudes are computed using the S-matrix method up to 6 MeV and using modified form factors from 6 MeV up to 20 MeV. Delbrück amplitudes were taken from Falkenberg's tabulations [11]. The GDR parameters, required for the nuclear resonance scattering, were extracted from the RIPL-3 database [12], and the neutron separation thresholds were obtained from NUDAT [13].

3.1.2 Validation procedures

An indication of the improvement in the modeling of the photon elastic scattering obtained with the current implementation with regard to the default GEANT4 implementation can be observed in Figure 3.1. This graph presents a comparison between simulated and experimental data for ^{238}U at 120 degrees for the 0.2–12 MeV energy interval. As expected, the low energy part of the graph is reproduced well by both implementations. However, differences between the two implementations start to appear at energies above 1 MeV and become significant at high energies.

Based on these results, an article was published in Nuclear Instruments and Methods in Physics Research Section B: Beam Interactions with Materials and Atoms [15].

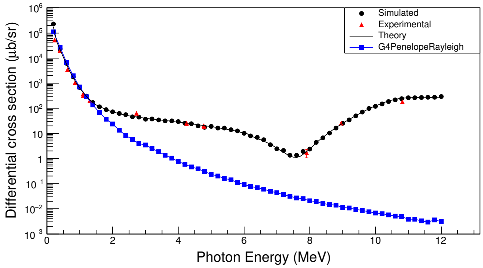

Figure 3.1: Elastic scattering differential cross-section (μb/sr) versus photon energy (MeV) for ^{238}U at a fixed scattering angle of 120 degrees. The full circles (black) are simulated points obtained from the current implementation. The continuous line (black) represents the theoretical data used for the current implementation. The square markers (blue) are simulated points obtained by using G4PenelopeRayleigh. The triangle markers (red) are experimental points obtained from Schumacher et al. [14].

3.2 Temporal analysis implementation

The temporal analysis of signals plays an integral part in nuclear spectroscopy. Regardless of the experiment, calibration source measurements or bunched-beam scenarios, the time overlap of signals (pile-up) will distort the measured spectra. The effects of pile-up can be observed as a loss in detection efficiency and the existence of improper counts in the spectra.

3.2.1 Pulse pile-up in digital electronics

The acquisition system used in this work is based on CAEN 725/730 digitizers. The digitizers run an FPGA based Digital Pulse Processing (DPP) algorithm in order to extract the energy and timing information from the digitized waveform. The pile-up rejection algorithm implemented in the DPP-PHA firmware can be divided into four cases of interest as shown in Figure 3.2.

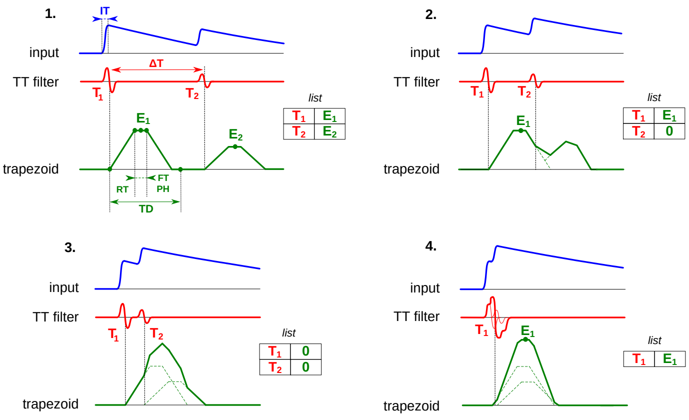

Figure 3.2: CAEN DPP-PHA pile-up rejection algorithm [16].

In an ideal situation, all photons will qualify for the first case, the scenario in which the recorded spectra will provide an exact, in terms of energy and count, representation of the photons that hit the detector. For the rest of the pile-up cases, the effects on the recorded spectra will be observed as a considerable loss in detection efficiency as the amount of pile-up rises. The scenario that shows the most significant disadvantage is the fourth case. In this particular instance, besides the loss in efficiency, the spectrum will contain events with invalid energies that are indistinguishable from proper events.

3.2.2 Geant4 implementation and validation

In order to account for the effects of pulse pile-up to simulated spectra, a model of the CAEN DPP-PHA pile-up rejection algorithm was implemented in Geant4. The testing and validation of the algorithm was made by using a 150% relative efficiency HPGe detector coupled to a DT5730 desktop digitizer. The experimental data was obtained with a ^{60}Co standard calibration source for multiple detector-source distances below 15 cm. The peak rate was the metric chosen in order to benchmark the implementation with respect to the experimental data. The most representative peaks for the validation were considered the peaks obtained purely from the summation of uncorrelated events, i.e. the 2.35 and 2.67 MeV peaks. Figure 3.3 shows the results of the validation for the 2.35 and 2.67 MeV rates for different input rise times.

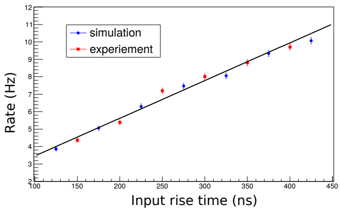

(a) 2.35 MeV

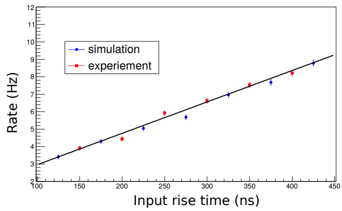

(b) 2.67 MeV

Figure 3.3: Peak rate versus the input rise time of the two ^{60}Co sum peaks, at a detector-source distance of 1 cm.

Chapter 4

Effective atomic number evaluation by using mono-energetic gamma rays

Established algorithms for dual-energy attenuation data analysis have been detailed in Section 2.1. The discrimination capabilities of dual-energy attenuation can be further improved through neural networks based algorithms. In this chapter, we explore two analysis methods for transmission radiography measurements using multi-monoenergetic photons and compare the quantitative benefits of neural networks against the dual-reflex method.

4.1 Single pixel analysis

In order to assess the feasibility of the neural network approach, the method is benchmarked against the dual-R method. Two data sets were used for this task, an experimental data set that was obtained by using proton-induced gamma rays and a simulated data set generated by using the Geant4 toolkit. The simulated data set was generated in similar conditions to the experimental measurements in order to assess the robustness of the methods against experimental uncertainties.

4.1.1 Gamma-rays production and the experimental setup

The generation of multiple gamma rays in the 1.7 – 12.3 MeV range was achieved by using two reactions of proton capture, listed in Table 4.1. The measurements were carried out at the 3MV Tandem accelerator of IFIN-HH [17]. The measurements were performed at a proton energy of 1.05 MeV in order to populate the 992 keV resonance of Al, which emits the 10.7 MeV gamma rays.

Reaction	$E_{\gamma 1}$	$E_{\gamma 2}$	$E_{\gamma 3}$	Q-value
			MeV	
$^{27}Al(p,\gamma)^{28}Si$	1.78	10.76	12.33	11.59
$^{19}F(p,\alpha\gamma)^{16}O$	6.13	6.92	7.12	8.12

Table 4.1: Proton capture reactions selected for the γ-ray production. The table lists the energies for the transitions of interest.

In order to assess the discriminating capabilities of the multiple gamma-ray attenuation method, six sample materials were selected: PE, Al, Cu, SL, W, and DU. To mimic a more realistic scenario, each sample was tested in three different configurations: without shielding, with SAE 304 stainless steel shield (SS), or lead shield. All the sample materials had an areal density of about 28.9 g/cm^2 except for the depleted uranium that had an areal density of about 50 g/cm^2.

4.1.2 Geant4 simulations

The purpose of the simulation was to generate data covering an extended range of Z values in similar conditions to the experimental measurements. A total number of 378 simulated points were obtained covering 42 values of Z with areal densities of 10, 20, and 30 g/cm^2 in three different configurations: without shield, with a SS shield, and with a lead shield.

4.1.3 Data processing

The analysis was performed based on the counts extracted from four regions of interest: 1.78, 6.13, 10.76, and 12.33 MeV. The counts were extracted with a fit procedure by using the sum function between a Gaussian and a first-order polynomial. A 70–30% training-testing data split configuration was selected for the model construction and performance assessment. A number of 2000 Monte Carlo cross-validation steps were performed in order to reduce the bias towards the test data set.

Dual-R approach

The training data were used to generate relative dual-energy reflexes for different combinations of extracted energies following the steps presented in Section 2.1.2. The training data was fitted by using equation (2.3), and the testing data was evaluated against the fitting curve.

Neural network approach

The single-pixel processing was based on a plain-feed-forward ANN configuration. The network was trained to model the correlation between the dual-energy gamma-ray attenuation and Z_{eff}. The networks were constructed by using the high-level neural networks application program interface Keras [18] running on top of TensorFlow [19]. The hyper-parameters tuning was done by using a random optimization strategy, part of Talos framework [20]. Two activation functions were selected for the model, Rectified Linear Units (ReLU) [21] for the hidden layers and sigmoid for the output layer. The ratio between the sample and the reference signal was used as input data with Z_{eff} as the label.

4.1.4 Results and discussions

The performance of the two models with respect to the Z_{eff} evaluation capabilities is shown in Table 4.2. Compared to the Dual-R model, the model based on neural networks shows a 48% improvement for the RMSE mean for the simulated data set and a 24% improvement for the RMSE mean for the experimental data set. The simplicity of the Dual-R model, coupled with several physical assumptions, limits the accuracy of this method. The model-independent approach and the increased complexity of the model give the edge to the ANN model.

Model	simulated		experimental	
	mean	std dev	mean	std dev
Dual-R	0.050	0.004	0.055	0.013
ANN	0.026	0.006	0.042	0.010

Table 4.2: The RMSE mean and its standard deviation resulted from the evaluation of the two methods for the experimental and simulated data sets.

4.2 2D analysis

Following the assessments of the two models on single-pixel attenuation data, the analysis is further extended to 2D transmission radiography. The performance of the models is evaluated based on the results obtained from two-dimensional transmission radiography data generated by using the Geant4 toolkit. The Z_{eff} prediction capabilities of the two methods are evaluated by using 500 validation input data points, composed of 1.7 and 10.7 MeV attenuation images.

4.2.1 Geant4 simulations

A two-dimensional scene was constructed for the 2D transmission radiography analysis. The scene was composed of multiple cylindrical or cuboidal shaped objects. The objects were positioned on two parallel layers, to allow multiple object attenuation. The geometrical parameters of the objects were arbitrarily assigned, the thickness was constrained to limit the areal density between 5 and 30 g/cm^2 for each layer. The atomic number of the objects was randomly allocated from 42 values covering the full range of the periodic table.

4.2.2 Data processing

Dual-R approach

The 2D processing for the dual-R method was done by using a pixel-by-pixel implementation. The dual-R curve was obtained by using the data set containing the 1500 simulated single-pixel transmission points. The pixel evaluation procedure was done following the procedure described in 4.1 for a 64×64 image obtained from the down-sampling of the 256×256 simulated images.

Neural network approach

The 2D processing was done by using a six-layered CNN. ReLU was selected as in-between layer activation, followed by batch normalization [22] and dropout layers. The number of filters for the convolutional layers was set to 50, using a 3×3 kernel with a (1,1) stride. The output of the network is handled by a two-channel convolutional layer followed by a sigmoid activation layer. The input and output were structured as a two-channel image with 64×64 pixels. The input images contained the ratio between the sample and the reference signals for the low and high energy attenuation. The labels were constructed by using normalized Z_{eff} and areal density values of the measured objects. The optimization of the weights and biases was done by using stochastic gradient descent (SGD) algorithm on a mean squared error loss function.

4.2.3 Results and discussion

A sample case for the 2D analysis procedure is shown in Figure 4.1. The panels of the first row contain the results obtained for the Z_{eff} evaluation procedure. A considerable difference can be observed in the quality of the ANN image with respect to the dual-R image, especially in the noise of the two images but also in the material discriminating power.

A plot of the Z_{eff} versus cluster index is shown in Figure 4.1 to better account for these differences. Note that the high uncertainties associated with the dual-R method lower its discriminat-

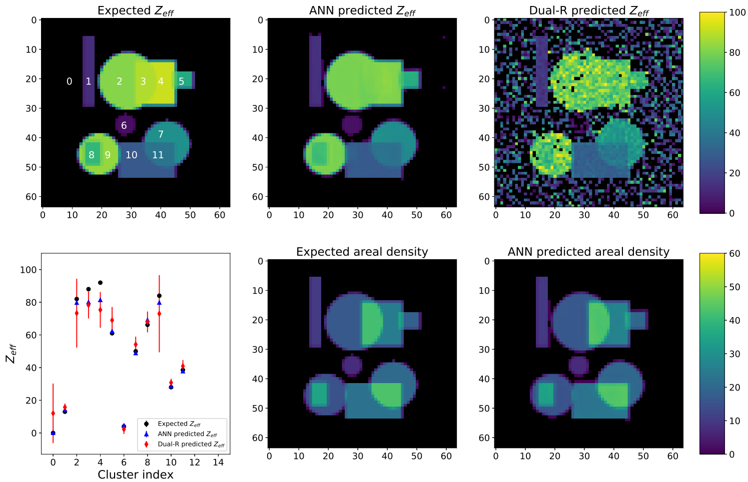

Figure 4.1: The results of the 2D processing analysis for one sample image part of the validation set. The first row contains the results of the Z_{eff} evaluation procedure, and shows the expected, ANN predicted, and dual-R predicted images. The second row contains a graph, which quantifies the Z_{eff} evaluation capabilities of both methods for all the clusters labeled in the image above. The last two panels contain the expected and ANN predicted image for the χ evaluation.

ing power for high-Z materials. On the contrary, the ANN-based method provides high-quality images with low pixel uncertainties and better discrimination power.

Based on these results, an article was published in The European Physical Journal Plus [23].

Chapter 5

Active cargo interrogation using NRF

The requirements for a high throughput isotopic analysis designed for cargo scanning are yet to be met. The potential improvements in gamma-ray beam quality powered by technological advancements of LCS machines may provide the solution to these problems. This chapter covers the advantages and drawbacks of the NRF based isotopic analysis by coupling a state-of-the-art LCS beam with a high-performance HPGe array.

5.1 Detection system

HPGe detectors are at the core of gamma-ray spectroscopy. The excellent energy resolution, detection efficiency, and relatively high counting rates make them the detectors of choice for the detection of photons in the keV up to tens of MeV range. One such array is now under development at the ELI-NP as part of the instrumentation proposed for photonuclear reactions using high intensity, quasi-monochromatic gamma-rays in the $0.2 - 20$ MeV range.

5.1.1 Clover detector based array - ELIADE

The ELIADE array is composed of eight clover HPGe detectors, with an eight-fold segmentation on each of the four crystals, and four $CeBr_3$ scintillator detectors. The segmented clover detectors, were characterized in terms of detection efficiency. Typical absolute detection efficiency measurements using standardized calibration sources, e.g. ^{60}Co or ^{152}Eu, can be used to characterize the detector up to 1.4 MeV. If higher energy efficiency is needed, short-lived sources, ^{56}Co or ^{66}Ga, or nucleon capture reactions (n,γ) or (p,γ), are required. The results of the detection efficiency validation procedures for one of the clover crystals, in the 0.5 – 11.6 MeV range, are shown in Figure 5.1. The simulated data reproduces the experimental data with good accuracy except for a slight overestimation at high energy that can be attributed to inaccuracies in the crystal modelling and the experimental measurement.

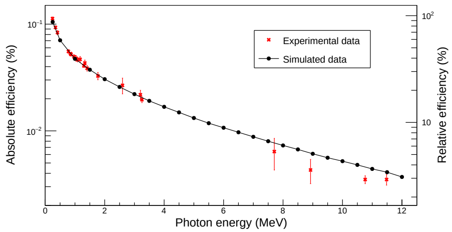

Figure 5.1: Absolute and relative detection efficiency of a HPGe clover detector's crystal. The red and black markers (linear interpolated - black line) represent the experimental and the simulated data for 0.5 - 11.6 MeV energy range. The measurements were made at a source-detector distance of 25 cm.

5.1.2 ELIADE performance for active interrogation measurements

The NRF spectrum, as recorded by the clover crystals over the full array, for the 2.176 MeV resonance of ^{238}U, is shown in Figure 5.2. The pile-up implementation is not enabled for this measurement in order to limit the complexity of the spectrum. The comparison between the ROI, around the 2.176 MeV peak, and the rest of the spectrum clearly shows that this type of measurement exhibits a low signal to background ratio. Most of the background is associated with the pair production and Compton scattering photons generated in the beam-sample interaction. The photons produced in the annihilation of the positrons have a substantial contribution to the total count rate; however, they cannot contribute to the ROI in the absence of signal pile-up. The spectral contribution of high energy Compton scattered photons to the ROI is prevented by placing the detectors at backward angles.

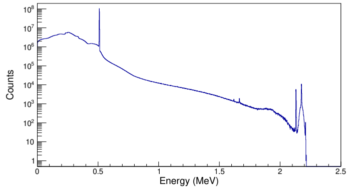

(a) full spectrum

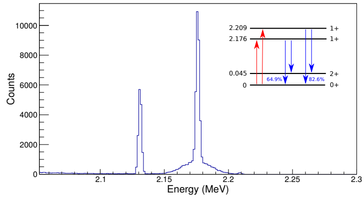

(b) ROI zoom

Figure 5.2: Simulated NRF spectrum for ^{238}U in the scattering configuration. The right side image details the spectrum and the nuclear level scheme for the 2–2.3 MeV range. The signal temporal analysis was disabled.

The only process that can significantly contribute as background on a spectral level to an NRF measurement is the elastic scattering of the incident beam. This effect is clearly depicted in Figure 5.2b, which details the 2 – 2.3 MeV range of Figure 5.2a. The elastic scattering contribution exhibits the spectral characteristics of the incident beam and can be observed at the base of the sharp 2.176 MeV peak, which corresponds to the ground state transition.

Enabling the signal pile-up model yields considerable differences in the simulated spectrum. The pile-up enabled alternative of Figure 5.2 is shown in Figure 5.3. The key distinction between the two spectra stands in the fact that the photons generated by pair production or Compton scattering can now contribute with counts to the full energy range of the spectrum due to the summation effect of the signal pile-up.

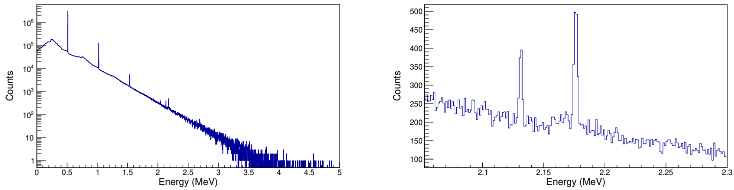

(a) full spectrum (b) ROI zoom

Figure 5.3: Simulated NRF spectrum for ^{238}U in the scattering configuration. The signal temporal analysis was enabled. Around 17% of the counts contained in the spectrum (left) are associated with a single-photon energy deposition.

5.2 Material discrimination by using NRF based isotopic mapping

Current technological constraints, in terms of beam quality and photon detection, restrict the NRF isotopic analysis to a low signal to background ratios. This effect has a direct influence on the measurement time, the detection limit, and the associated uncertainty. As it stands, the method does show practical difficulties for samples that require large scanning regions. One possible mitigation requires coupling the NRF isotopic analysis to high throughput complementary methods that are able to limit the required scanning area.

5.2.1 NRF based 2D imaging

A high Z_{eff} region containing clusters 1, 2, 3, 4, and 5, shown in Figure 4.1, was selected for the ^{238}U isotopic mapping. This analysis intends to isolate clusters 3 and 4, which contain the isotope of interest, from all the other clusters from the scene. The region of interest was scanned by using a pencil beam implementation on a 19×13 grid with a 0.4 cm pixel for a total surface of 7.6×5.2 cm^2. The generated image quality was assessed by using the contrast-to-noise (CNR) ratio.

The typical procedure for highlighting the ^{238}U containing region from the measured rates requires calculating the pixel-by-pixel ratio between an intensity proportional image and the NRF image. The ratios between 0.511 MeV and NRF images for increasing measurement times are shown in Figure 5.4. Upon the 0.511 MeV rate normalization, the generated images include only the clusters containing the isotope of interest. The measurement times were selected in order to achieve CNR values that cover the 1–3 range.

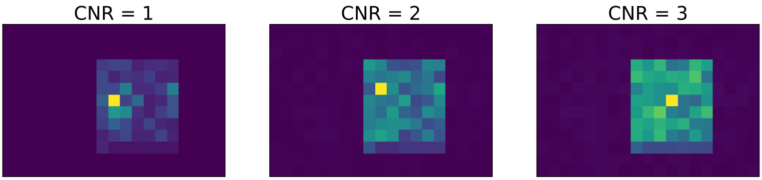

Figure 5.4: The ratio between the 0.511 MeV peak and NRF rate for increasing measurement time, for resulting CNR values between 1 and 3.

5.2.2 Areal density

Depending on the application, an areal density evaluation for the isotope of interest may also be required. An approach based on a Monte Carlo generated calibration curve is shown in Figure 5.5. The curve shows the areal density variation versus $\mathbb{A}$, parameter based on spectral data, calculated as [24]:

$$\mathbb{A} = \frac{R^{NRF}_{obj}}{R^{NRF}_{no\ obj}} \times \frac{R^{pair}_{no\ obj}}{R^{pair}_{obj}}, \tag{5.1}$$

where R^{NRF} and R^{pair} are the rates for the NRF and 0.511 MeV peaks for measurements with and without the object. The pair production normalization factor accounts for the non-resonant attenuation and fluctuations in the beam intensity. For the cases in which the normalization error exceeds the expected accuracy, precise measurements for the beam intensity are required, which is the subject of Section 5.3.

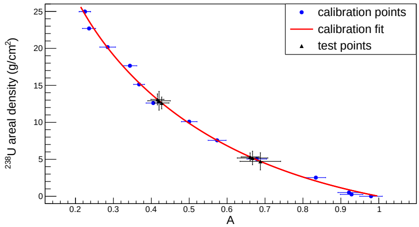

Figure 5.5: Monte Carlo based areal density evaluation curve for ^{238}U. $\mathbb{A}$ is the normalized ratio between the NRF rates with and without the object calculated using equation (5.1).

5.3 Gamma beam intensity measurement

Measuring the spatial, spectral, and temporal characteristics of γ-ray beams has been a longstanding problem since the early development of the γ-ray beam facilities. One instrument proposed for measuring the beam intensity and energy parameters is based on a large volume HPGe detector with an anti-Compton shield. In this section, we investigate the use of Compton scattering for continuously measuring the intensity and energy of the γ-ray beam at ELI-NP based on test experiments at HIγS.

5.3.1 Beam energy and intensity measurements at HIGS

The difficulties associated with an accurate evaluation of the intensity has led to the development of several absolute and relative methods. This section will focus on a Compton scattering approach based on histogram matching between experimental and simulated spectra. In order to validate this, we analyzed experimental data acquired at HIGS, for the 4.5 – 10 MeV range, and compared the results with ^{197}Au activation and paddle detector measurements.

Compton scattering method

The differential cross-section for Compton scattering can be calculated by using the well-known Klein-Nishina expression [25]. If the geometrical characteristics of the setup and the parameters of the scatterer are known, the equation can be used to calculate the incident intensity from the number of scattered photons. This method requires the placement of an in-beam scattering target from which the incident photons will scatter into a detector placed at a predefined angle with respect to the beam axis.

Experimental setup

A 120% efficient co-axial HPGe detector [26] was used to make measurements of the beam energy, energy spread, and intensity. The motorized system could move the detector directly in the path of the γ-ray beam (the 0° position) or at an angle outside the path of the beam. Although the head of the HPGe detector was placed inside the anti-Compton shield, the anti-coincidence setup was not operational for this experiment. A copper collimator (11.43-cm long, 5.08-cm outside radius, and 0.953-cm hole radius) was positioned in front of the HPGe detector to define the scattering angle and reduce the background rate.

Geant4 simulations

The HPGe detector reproduction was based on the detector's technical drawings provided by the manufacturer. One of the important parameters of the experimental setup that could not be precisely inferred from the experiment was the position of the beam spot on the face of the detector. The best reproduction of the experimental data is obtained when the beam hits the face of the detector 2.7 cm off the center of the detector, position that yields good agreement for all the energy cases available for this analysis.

The spatial characteristics of the beam were inferred from images captured using a CCD camera.

Gamma beam energy measurement

The energy parameters of the beam were determined for several discrete energies in the 4.5 to 10 MeV range by using in-beam measurements. A two-step procedure was applied in order to obtain the γ-ray beam parameters. In the first step, a normal distribution fit of the full absorption peak was performed in order to determine an initial value for the energy parameters, i.e. full-width half maximum (FWHM) and centroid. In the second step of the procedure, we simulated the detector's response to a beam with the energy parameters obtained from the fit. Slight adjustments were made to the beam parameters in order to obtain the best agreement between simulation and experiment. The results of the analysis procedure for the 4.5 – 10 MeV range are presented in Figure 5.6a. The plot shows a linear dependence between the calculated and the expected energies, given by the accelerator parameters.

Intensity measurement using Compton scattering

In order to determine the intensity of the γ-ray beam, the HPGe was moved out of the beam path, and the attenuator was removed. A collimator was added in front of the detector in order to limit the angular range of the scattered photons. The simulated spectra for the Compton scattering configuration were obtained by using the energy parameters calculated in Section 5.3.1. Once a good agreement is obtained between the simulated and experimental spectra, the intensity of the beam can be calculated by using the number of photons that were required to generate the simulated spectrum and the acquisition time of the measurement. The results of such analysis are presented in Figure 5.6b together with beam intensity values obtained from a paddle detector [27] situated upstream from the experimental setup.

There is good agreement between the beam intensity values obtained by using Compton scattering and the paddle detector except

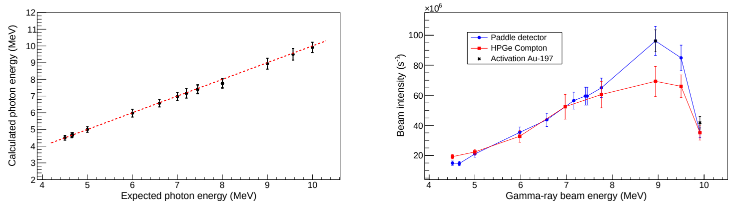

(a) Energy measurement

(b) Intensity measurement

Figure 5.6: Beam energy and intensity results for the 4.5–10 MeV range. The energy FWHM is shown as uncertainty for the calculated data. The beam intensity results were obtained by using Compton scattering, paddle detector, and ^{197}Au activation measurements.

for 9 and 9.57 MeV. The two runs at 9 and 9.57 MeV have the highest dead times in the HPGe detector.

5.3.2 Proposed instrument at ELI-NP

A similar setup for intensity and energy measurements was proposed at ELI-NP. The setup is composed of a detection assembly that contains a 150% relative efficiency HPGe coupled to a NaI(Tl) anti-Compton shield, a positioning system that allows rotation and translation with respect to the scattering target and a support structure for the ensemble.

In order to characterize and optimize the proposed instrument for energy and intensity measurements, an accurate reproduction of the setup was constructed by using the Geant4 simulation toolkit. In order to extend the efficiency measurements up to 11.6 MeV proton-capture reactions on ^{23}Na and ^{27}Al and standard calibration sources, ^{60}Co, ^{56}Co, and ^{152}Eu were used. Figure 5.7 presents the measured efficiency of the 150% HPGe together with the simulated efficiency.

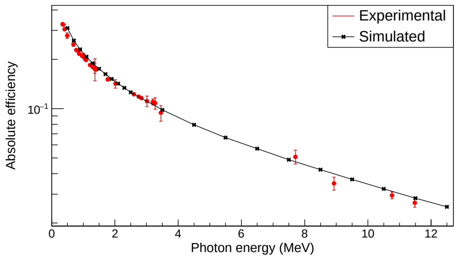

Figure 5.7: Absolute efficiency of a 150% HPGe detector. The red and black markers represent the experimental and the simulated data for the 1-12 MeV range.

Based on these results, an article was published in Nuclear Instruments and Methods in Physics Research Section A: Accelerators, Spectrometers, Detectors and Associated Equipment [28].

Conclusions

This thesis investigated the potential advantages and drawbacks of NRF isotopic mapping powered by quasi-monochromatic gamma-ray beams. The analysis was performed by using an enhanced Monte Carlo framework constructed on top of the base functionalities of Geant4 to provide improved estimates for NRF measurement outcomes. Several topics were targeted throughout this work, ranging from the evaluation of NRF measurement outcomes to associated aspects as ROI selection and beam intensity measurements. The topics were approached from a Monte Carlo standpoint, validated in most cases by using theoretical or experimental data. One of the targets of this work was to build the framework required to generate accurate estimates to be used as starting points for future experimental designs.

The first part of this work presents the Geant4 implementation of the photon elastic scattering covering the 0.3 MeV to 20 MeV energy range for all atomic numbers. The implementation was done by using a complete theoretical framework to account for the interference effects between the processes involved in the scattering cross-section. With the use of the S-matrix formalism, new scattering amplitudes were calculated for Rayleigh scattering to extend the cross-section data table. A validation procedure employed for a significant number of test cases showed good agreement between the simulated, experimental, and theoretical data. The current model best reproduces the experimental data for scattering angles above 90 degrees, which is the angular domain of interest in the detection of NRF rays for fundamental nuclear physics as well as for NRF-based applications.

An additional component with a considerable influence on the spectral background of a typical NRF measurement is the signal pile-up. The signal pile-up implementation was required in order to assess the effect of pulse pile-up on the measured spectrum and to generate accurate estimates for the expected counting rates. In order to quantify the distortion associated with this effect, the digital acquisition chain proposed for the ELIADE array was modeled and implemented as part of the simulation code. Experimental validation data were acquired by using a well-characterized 150% HPGe detector and a standard ^{60}Co calibration source. The results of the validation procedure based on peak counting rates, for the gamma lines and the associated sum peaks, showed good agreement between simulated and experimental data.

Further on, the focus of the work shifted to ROI selection techniques, based on dual-energy attenuation, required to manage the practical limitations of NRF based isotopic mapping. A novel dual-energy attenuation data analysis procedure based on artificial neural networks was proposed. The neural network-based model was compared with the relative dual-energy reflex for simulated and experimental data sets. For this comparison, a single-pixel experimental data set for photons in the 1.7–12.3 MeV range, obtained by using proton-capture reactions on composite targets, was supplemented with a Geant4 based data set. A considerable advantage was demonstrated for the neural network approach with improvements, in terms of RMSE, of about 48% and 24% for simulated and experimental data. The analysis was further extended to the processing of simulated dual-energy transmission radiography images. A large number of 2D scenes, containing randomly selected cylindrical and cuboidal shaped objects, were generated to be used as a training-validation data set. For the 2D scenes, a direct image analysis was employed by using a convolutional neural network and compared it with the pixel-by-pixel approach for the dual-energy reflex. The evaluation procedure showed a considerable advantage for the neural network approach in terms of image quality, evaluation error, and the associated uncertainty.

In the final part of the thesis, the analysis focused on the particularities of NRF-based active cargo interrogation. The work highlighted the advantages and drawbacks of coupling a state-of-the-art LCS beam with a high-performance HPGe array for the detection of ^{238}U. The clover detectors, part of ELIADE array, were modeled inside the Geant4 framework and were validated in terms of detection efficiency and temporal signal analysis. On the detection efficiency side, the clover crystals were validated by using experimental data for photon energies up to 12 MeV, obtained through proton-capture reactions. In terms of temporal signal analysis, the clover crystals were validated by using ^{60}Co peak counting rates for the gamma lines and associated sum peaks. The validation procedures showed good agreement between the experimental data and the implemented representation of the clover detector. Following the implementation, a setup optimization phase investigated the spectral characteristics, the ROI background, and the pile-up to total ratio. This analysis generated an optimal value for the passive shielding thickness based on an NRF peak rate optimization. The next step of the analysis covered the results of a raster scan procedure aimed at highlighting objects containing ^{238}U from of a high Z_{eff} scene. On the image quality side, the results point to the fact that the theoretical contrast-to-noise ratio minimum value of 3 can be achieved only for high ^{238}U concentrations. However, a contrast-to-noise ratio value of 1, which is associated with a discernible object, can be obtained for ^{238}U concentrations as low as 1%.

A Monte Carlo calibration curve approach was considered for the areal density evaluation procedure. The evaluation capabilities of the calibration curve were assessed against simulated data obtained for several test cases, which showed adequate results compared to the expected values. The areal density assessment was made under a fixed beam intensity assumption. However, for an actual experimental scenario, knowledge of the beam intensity is essential, which is the focus of the last part of the chapter. The final section investigates the possibility of measuring the energy and intensity of a gamma-ray beam by using an HPGe detector. For method development and validation purposes, an experimental data set containing HPGe measurements were acquired at HIGS for photon energies in the 4.5–10 MeV range. The HPGe measurements were made in two different configurations: in-beam measurements for the energy evaluation and off-beam measurements for Compton scattering based intensity evaluation. The data analysis was based on a histogram matching approach that compared experimental and simulated spectra in order to extract the beam parameters.

In terms of beam energy, the method showed excellent results with respect to the expected values for the selected energy range. On the beam intensity side, the results of the Compton-based method were compared with ^{197}Au activation and paddle detector measurements. Good agreement was observed, except for the 9 and 9.57 MeV points for which the method underestimates the actual values. The errors were attributed to the significant dead time in the acquisition chain for the experimental measurements.

As it stands, an NRF-based isotopic analysis does provide the capability to identify small isotopic quantities inside high Z_{eff} samples. However, the method does show significant practical limitations due to the relatively long measurement time. While significant upgrades in terms of detection efficiency, background reduction, and data analysis can still be achieved, improvements to the beam bandwidth would translate the best to shorter measurement times. Two orders of magnitude increase in terms of the NRF count rate would allow the method to be practical for large scenes or more complex 3D mappings.

The presented work enables several possibilities for follow-up research. Concerning data analysis, several algorithms have the potential to simplify or augment the data analysis procedure. Neural-network based tools have shown promising results for automatic spectral analysis and image processing. Besides these, other signal processing techniques aimed at reducing the data acquisition time, such as compressed sensing, are yet to be investigated in the context of NRF isotopic mapping. On the setup configuration side, an additional analysis based on standard detectors for applications such as NaI, CsI, and PVT, which have low maintenance costs, can yield estimates oriented to practical implementations. Such a setup could be used to generate a minimal set of LCS parameters required to enable the NRF isotopic mapping for high throughput scanning systems.

Bibliography

[1] `www.eli-np.ro`, 2019.

[2] C. A. Ur *et al.*, Rom. Rep. Phys. **68**, S483 (2016).

[3] F. Camera *et al.*, Rom. Rep. in Phys. **68**, S539 (2016).

[4] G. Suliman *et al.*, Rom. Rep. Phys. **68**, S799 (2016).

[5] M. J. Berger *et al.*, XCOM: Photon cross section database, 2010.

[6] S. V. Naydenov, V. D. Ryzhikov, and C. F. Smith, Nucl. Instr. Meth. A **537**, 462 (2005).

[7] W. Bertozzi and R. J. Ledoux, Nucl. Instr. and Meth. B **241**, 820 (2005).

[8] S. Agostinelli *et al.*, Nucl. Instr. and Meth. A **506**, 250 (2003).

[9] X-5 Monte-Carlo Team, MCNP - A General N-Particle Transport Code - LA-UR-03-1987, 2003.

[10] M. Batic, G. Hoff, M. Pia, and P. Saracco, IEEE Trans. Nucl. Sci **59**, 1636 (2012).

[11] H. Falkenberg *et al.*, Atom. Data Nucl. Data **50**, 1 (1992).

[12] R. Capote *et al.*, Nucl. Data Sheets **110**, 3107 (2009).

[13] R. Kinsey *et al.*, The NUDAT/PCNUDAT Program for Nuclear Data, paper submitted to the 9th International Symposium of Capture Gamma-ray Spectroscopy and Related Topics, 1996.

[14] M. Schumacher, P. Rullhusen, F. Smend, W. Mücknheim, and H. G. Börner, Nucl. Phys. A **346**, 418 (1980).

[15] G. V. Turturica, V. Iancu, G. Suliman, and C. A. Ur, Nucl. Instr. and Meth. B **436**, 68 (2018).

[16] CAEN, MC2Analyser User Manual rev. 5, 2017.

[17] D. G. Ghita *et al.*, Proc. of HIAT , TUB02 (2012).

[18] F. Chollet *et al.*, Keras, 2015.

[19] M. Abadi *et al.*, TensorFlow: Large-scale machine learning on heterogeneous systems, 2015, Software available from tensorflow.org.

[20] M. Kotila, Talos, 2018.

[21] A. F. Agarap, Deep Learning using Rectified Linear Units (ReLU), 2018, arXiv:1803.08375.

[22] S. Ioffe and C. Szegedy, ICML'15 Proceedings of the 32nd International Conference on Machine Learning **37**, 448 (2015).

[23] G. V. Turturica *et al.*, EPJ Plus **135**, 140 (2020).

[24] B. J. Quiter, B. A. Ludewigt, V. V. Mozin, C. Wilson, and S. Korbly, Nucl. Instr. and Meth. B **269**, 1130–1139 (2011).

[25] O. Klein and T. Nishina, Z. Phys. **52**, 853 (1929).

[26] M. Blackston, Ph.D. thesis, Duke University (unpublished), 2007.

[27] R. E. Pywell, O. Mavrichi, W. A. Wurtz, and R. Wilson, Nucl. Instr. and Meth. A **606**, 517 (2009).

[28] G. V. Turturica *et al.*, Nucl. Instr. and Meth. A **921**, 27 (2019).